Nanocatalysis

DOI: 10.1002/anie.201103698

Crystal-Plane-Controlled Surface Restructuring and Catalytic Performance of Oxide Nanocrystals**

Huizhi Bao, Wenhua Zhang, Qing Hua, Zhiquan Jiang, Jinlong Yang, and Weixin Huang**

Industrial catalysts usually consist of nanoparticles exposing different crystal planes and atomic terminations that play an important role in their catalytic performance.[1,2] Catalysts for heterogeneous catalytic reactions operate under pressures up to several hundred atmospheres and at temperatures up to several hundred degrees Celsius, so that the catalyst nanoparticles can easily undergo surface restructuring to adopt the thermodynamically most stable structure. Thus, it is crucial to explore the restructuring process of catalyst surfaces under the reaction conditions to understand catalytic processes at the microscopic level; moreover, it is desirable to tune the catalytic performance of the catalyst nanoparticles by controlling the surface restructuring process in reactive atmospheres.

The direct study of catalyst nanoparticles is challenging because of the complexity of their structures. Model catalysts such as single crystals and vicinal surfaces have been extensively investigated to understand the surface restructuring phenomenon, and these studies have provided deep insights. Strongly chemisorbed adsorbates are well known to induce structural changes to metal surfaces.[3–5] More profound restructuring of metal surfaces has been demonstrated to be driven by the formation of dense adsorbate layers,[6–8] moreover, it has been argued that the catalytic activities of Ru, Rh, Pd, and Ag in oxidation reactions are related to ultrathin oxide films on their surfaces.[6,7,9–13] Recently, microscopic and spectroscopic experimental results[14–20] have directly revealed changes in the surface structure of metal nanoparticles and changes in both the surface structure and surface composition of bimetallic nanoparticles in reactive atmospheres. Reactive gases can also change the structure and composition of oxide nanoparticles to form a catalytically active surface phase in situ.[21,22] Thus, the concept of surface restructuring of catalyst nanoparticles during heterogeneous catalysis reactions has been well accepted, and therefore a challenging and inspiring task is to further explore whether such surface restructuring processes can be controlled and utilized as a novel strategy to improve and design efficient nanocatalysts.

In the present study, in which CO oxidation catalyzed by uniform Cu_2O nanocrystals with different well-defined structures is employed as a model system, we not only clearly demonstrate that the in situ formed CuO thin film on the Cu_2O nanocrystals is responsible for their catalytic activity but also unambiguously identify the key role of the crystal plane exposed on the Cu_2O nanocrystals in the surface restructuring process. Our findings revealed the novel concept that the surface restructuring process of catalyst nanoparticles and the structure and catalytic performance of the restructured surface can be controlled by engineering the shape of the nanoparticles and the exposed crystal plane.

Uniform octahedral (o-Cu_2O) and cubic (c-Cu_2O) Cu_2O nanocrystals were synthesized by means of solution-phase methods.[23] SEM, TEM, and HRTEM images (see Figure S1 in the Supporting Information) demonstrate that o-Cu_2O nanocrystals with diameters of 600–800 nm and c-Cu_2O nanocrystals with diameters of 700–900 nm exclusively expose the {111} and {100} crystal planes, respectively. The XRD patterns of the o-Cu_2O and c-Cu_2O nanocrystals (Figure 1 A) confirm their bulk crystal phase to be a face-centered-cubic (fcc) Cu_2O structure (JCPDS card No. 78-2076). The Cu $2p_{3/2}$ binding energies of o-Cu_2O and c-Cu_2O (Figure 1 B) locate at $\approx$931.8 eV, which is a characteristic value for Cu^I, thus demonstrating that their surfaces do not get oxidized under ambient conditions.

Figure 2 A shows the catalytic performance of o-Cu_2O and c-Cu_2O for CO oxidation. o-Cu_2O is much more active than c-Cu_2O. o-Cu_2O becomes active at 150 °C and achieves a CO conversion of 91.5 % at 240 °C, whereas c-Cu_2O only becomes active at 190 °C and achieves a CO conversion of 45.1 % at 240 °C. Structures of the o-Cu_2O and c-Cu_2O nanocrystals used in the catalytic activity evaluation up to 240 °C, defined as CuO/o-Cu_2O and CuO/c-Cu_2O, respectively, were then characterized. The XRD patterns (Figure 1 A) demonstrated that the bulk crystal phase of CuO/o-Cu_2O and CuO/c-Cu_2O

[*] H. Bao,[+] Q. Hua, Dr. Z. Jiang, Prof. Dr. W. Huang
Hefei National Laboratory for Physical Sciences at the Microscale
CAS Key Laboratory of Materials for Energy Conversion and Department of Chemical Physics
University of Science and Technology of China
Jinzhai Road 96, Hefei 230026 (China)
E-mail: huangwx@ustc.edu.cn
Dr. W. Zhang[+]
CAS Key Laboratory of Materials for Energy Conversion and Department of Materials Science and Engineering
University of Science and Technology of China
Jinzhai Road 96, Hefei, 230026 (China)
Prof. Dr. J. Yang
Hefei National Laboratory for Physical Sciences at the Microscale and Department of Chemical Physics
University of Science and Technology of China
Jinzhai Road 96, Hefei 230026 (China)
E-mail: jlyang@ustc.edu.cn
[+] These authors contributed equally to this paper.

[**] This work was financially supported by the National Natural Science Foundation of China (21173204, 11079033), the National Basic Research Program of China (2010CB923302, 2011CB921404), the Fundamental Research Funds for the Central Universities, and the MPG-CAS partner group program.

Supporting information for this article is available on the WWW under http://dx.doi.org/10.1002/anie.201103698.

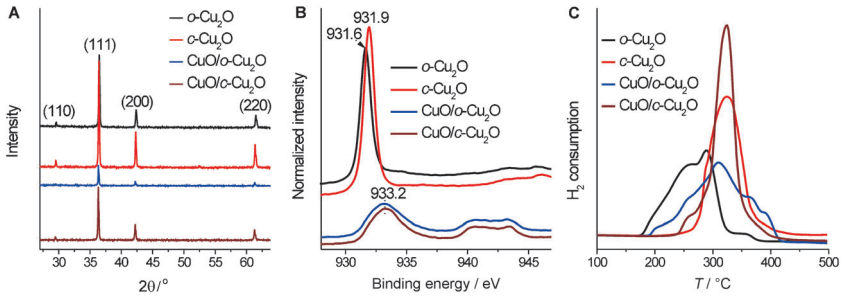

Figure 1. A) XRD patterns, B) Cu $2p_{3/2}$ XPS spectra, and C) H_2 temperature-programmed reduction profiles of *o*-Cu_2O, *c*-Cu_2O, CuO/*o*-Cu_2O, and CuO/*c*-Cu_2O.

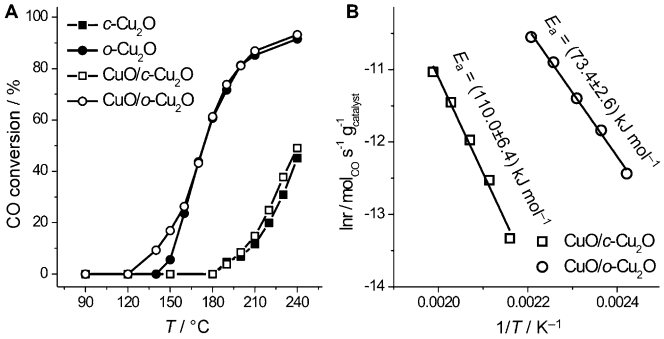

Figure 2. A) Catalytic performance of *o*-Cu_2O, *c*-Cu_2O, CuO/*o*-Cu_2O, and CuO/*c*-Cu_2O in the oxidation of CO. B) The Arrhenius plot of the oxidation of CO catalyzed by CuO/*o*-Cu_2O and CuO/*c*-Cu_2O.

still remain as the fcc Cu_2O structure. However, only the Cu^{II} feature with the Cu $2p_{3/2}$ binding energy at 933.2 eV and a doublet shoulder appear in the Cu $2p_{3/2}$ XPS spectra of CuO/*o*-Cu_2O and CuO/*c*-Cu_2O, and the Cu^{I} feature observed in the *o*-Cu_2O and *c*-Cu_2O spectra completely disappears, clearly demonstrating the existence of a CuO thin film on the surface of CuO/*o*-Cu_2O and CuO/*c*-Cu_2O (Figure 1B). The N 1s XPS spectra of *o*-Cu_2O and CuO/*o*-Cu_2O (Figure S2 in the Supporting Information) show that the poly(vinylpyrrolidone) (PVP) capping agent on *o*-Cu_2O introduced during the sample preparation process is removed during the catalytic activity evaluation in CO oxidation up to 240 °C. Meanwhile, CuO/*o*-Cu_2O and CuO/*c*-Cu_2O exhibit H_2-TPR profiles (Figure 1C) different from the corresponding *o*-Cu_2O and *c*-Cu_2O H_2-TPR profiles, also indicating their different surface structures.

SEM images (Figure S3A & B in the Supporting Information) show that the shape of CuO/*o*-Cu_2O and CuO/*c*-Cu_2O is still octahedral and cubic, respectively, but TEM images (Figure S3C & D in the Supporting Information) show that, compared with *o*-Cu_2O and *c*-Cu_2O (Figure S1 in the Supporting Information), CuO/*o*-Cu_2O and CuO/*c*-Cu_2O possess rounder corners and rougher surfaces. High-resolution TEM images of CuO/*o*-Cu_2O and CuO/*c*-Cu_2O (Figure 3 and Figure S4 & S5 in the Supporting Information) clearly reveal that their surface structure differs from their bulk structure. The lattice fringe structure resolved in the inner region of CuO/*c*-Cu_2O (Figure 3B) and CuO/*o*-Cu_2O (Figure 3E) is identical to that of the corresponding *c*-Cu_2O (Figure S1C in the Supporting Information) and *o*-Cu_2O (Figure S1F in the Supporting Information), thus demonstrating that the bulk CuO/o-Cu2O and CuO/c-Cu2O remain as octahedral and cubic Cu_2O nanocrystals, respectively. The surface region of CuO/*c*-Cu_2O (Figure 3C) gives two sets of lattice fringes of 0.25 and 0.23 nm with an intersection angle of 67°; these lattice fringes respectively correspond to the lattice fringe of the (002) and (111) planes of a monoclinic CuO structure (JCPDS card No. 89-5897). The lattice fringe of 0.28 nm of the surface region of CuO/*o*-Cu_2O corresponds to the lattice fringe of the (110) plane of monoclinic CuO structure. Thus, CuO/*o*-Cu_2O and CuO/*c*-Cu_2O have Cu_2O nanooctahedra (core)/CuO (shell) and Cu_2O nanocube (core)/CuO (shell) structures, respectively. The thickness of the CuO shell is ≈10 nm in CuO/*o*-Cu_2O and ≈6–10 nm in CuO/*c*-Cu_2O, as estimated from the TEM images.

The surfaces of *o*-Cu_2O and *c*-Cu_2O do not get oxidized under ambient conditions, therefore it can be concluded that *o*-Cu_2O and *c*-Cu_2O both undergo surface restructuring to form CuO thin films in situ during the catalytic CO oxidation at temperatures up to 240 °C. Next we evaluated the catalytic performance of CuO/*o*-Cu_2O and CuO/*c*-Cu_2O in CO oxidation at temperatures up to 240 °C (Figure 2A). Similar to the Cu_2O nanocrystals, CuO/*o*-Cu_2O is much more active than CuO/*c*-Cu_2O. CuO/*o*-Cu_2O becomes active at 140 °C and achieves a CO conversion of 93.2 % at 240 °C, whereas CuO/*c*-Cu_2O only becomes active at 190 °C and achieves a CO conversion of 49.1 % at 240 °C. The catalytic behaviors of *o*-

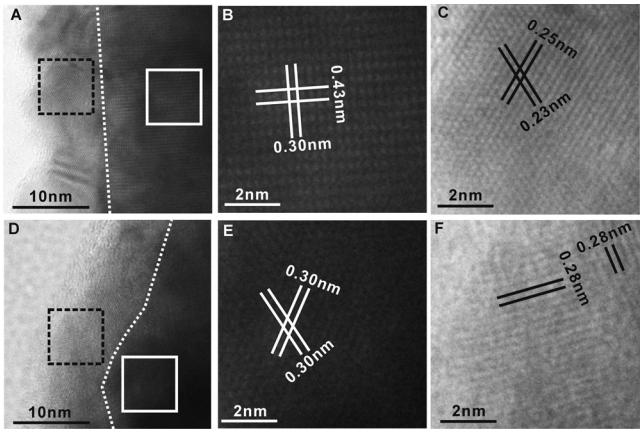

Figure 3. A) High-resolution TEM image of CuO/*c*-Cu_2O in Cu_2O [$1\bar{1}0$] view. B) Enlarged high-resolution TEM image of the inner region of CuO/*c*-Cu_2O indicated by the solid white square in (A). C) Enlarged high-resolution TEM image of the surface region of CuO/*c*-Cu_2O indicated by the dash black square in (A). D) High-resolution TEM image of CuO/*o*-Cu_2O in Cu_2O [$1\bar{1}\bar{1}$] view. E) Enlarged high-resolution TEM image of the inner region of CuO/*o*-Cu_2O indicated by the solid white square in (D). F) Enlarged high-resolution TEM image of the surface region of CuO/*o*-Cu_2O indicated by the dash black square in (D). The dashed white lines in (A) and (D) indicate the CuO-Cu_2O boundary in CuO/*c*-Cu_2O and CuO/*o*-Cu_2O, respectively.

Cu_2O and *c*-Cu_2O are similar to those of the corresponding CuO/*o*-Cu_2O and CuO/*c*-Cu_2O, thus suggesting that the CuO thin film formed in situ during the catalytic oxidation of CO is responsible for the catalytic activity for all the catalysts. The catalytic activities of *o*-Cu_2O and CuO/*o*-Cu_2O differ at temperatures below 160 °C, thus indicating that the active CuO thin film fully develops on the surface of the octahedral Cu_2O nanocrystals at ≈160 °C during the course of the first cycle of the catalytic activity evaluation. Figure 2B shows the Arrhenius plot of CO oxidation catalyzed by CuO/*o*-Cu_2O and CuO/*c*-Cu_2O, from which the apparent activation energies were calculated to be 73.4 ± 2.6 and 110.0 ± 6.4 kJ mol^{-1}, respectively. This result indicates that the CO oxidation catalyzed by the CuO thin film of CuO/*o*-Cu_2O and the CO oxidation catalyzed by the CuO thin film of CuO/*c*-Cu_2O involve different catalytically active sites and proceed with different reaction mechanisms.

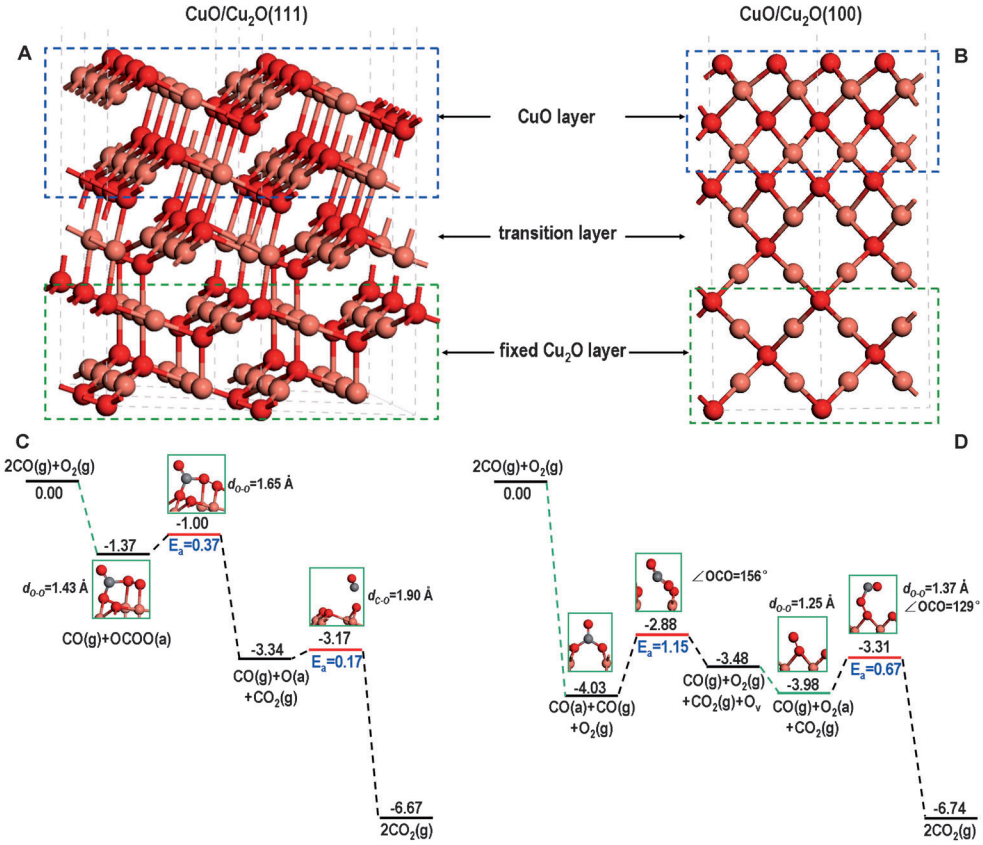

Figure 4. Optimized geometric structures of CuO/Cu_2O(111) (A) and CuO/Cu_2O(100) (B) surfaces, and the energy profiles of each elementary step in CO oxidation catalyzed by CuO/Cu_2O(111) (C) and CuO/Cu_2O(100) (D) surfaces. The red, pink, and grey spheres represent O, Cu, and C atoms, respectively.

Density functional theory (DFT) calculations were performed using the experimentally observed structures as the starting point. The CuO overlayer was constructed and optimized on Cu_2O (111) and (100) surfaces to model CuO/*o*-Cu_2O and CuO/*c*-Cu_2O, respectively. We previously reported that the optimized surface structure of Cu_2O(111) is different from that of Cu_2O(100) (Figure S6 in the Supporting Information); coordinated unsaturated Cu atoms are present on Cu_2O(111) but not on Cu_2O(100).[23] Interestingly, the crystal plane exposed on the Cu_2O substrate controls the surface structure of the resulting CuO overlayer. The CuO overlayer on Cu_2O(111) (Figure 4A) is terminated with three-coordinated Cu (Cu_{3c}) and three-coordinated oxygen (O_{3c}) atoms while the CuO overlayer on Cu_2O(100) (Figure 4B) is terminated only with O_{2c} atoms.

DFT calculation results demonstrate that CO oxidation catalyzed by the CuO thin film on Cu_2O(111) and CO oxidation catalyzed by the CuO thin film on Cu_2O(100) involve different types of catalytically active sites and proceed with different reaction mechanisms. On the CuO/Cu_2O(111) surface (Figure 4C and Table S1 in the Supporting Information) the individual adsorption of CO and O_2 on the Cu_{3c} sites is quite weak, but the co-adsorption of CO and O_2 on Cu_{3c} and O_{3c} sites is quite strong and forms a OCOO(a) surface intermediate. Then the OCOO(a) surface intermediate decomposes to produce a O(a) adatom and CO_2 with an activation energy of 0.37 eV and finally CO reacts with the O(a) adatom to produce CO_2 with an activation energy of 0.17 eV, thus completing the catalytic reaction cycle. Thus, the elementary step with the largest activation energy in CO oxidation catalyzed by the CuO overlayer on Cu_2O(111) is the decomposition of the OCOO(a) surface intermediate with an activation energy is 0.37 eV.

On the CuO/Cu_2O(100) surface (Figure 4D and Table S1 in the Supporting Information), O_2 cannot chemisorb on the O_{2c}-terminated surface, but CO binds with O_{2c} sites very strongly to form the CO_3(a) surface intermediate. Then the CO_3(a) surface intermediate decomposes to produce CO_2, thus creating an oxygen vacancy in CuO with an activation energy of 1.15 eV; this is a typical Mars-Van Krevelen mechanism. Next O_2 can chemisorb on the oxygen vacancy site in CuO to form O_2(a), and finally CO reacts with O_2(a) to produce CO_2 with an activation energy of 0.67 eV, thus refilling the oxygen vacancy and completing the catalytic reaction cycle. Therefore the elementary step with the largest activation energy in the CO oxidation catalyzed by the CuO overlayer on Cu_2O(100) is the decomposition of the CO_3(a) surface intermediate with an activation energy is 1.15 eV. These DFT calculation results agree quite well with experimental results, which show that CO oxidation catalyzed by

$CuO/o\text{-}Cu_2O$ proceeds with a lower apparent activation energy than that catalyzed by $CuO/c\text{-}Cu_2O$.

Thus, under the same reaction conditions as for CO oxidation, the surface restructuring process of Cu_2O nanocrystals and the structure and catalytic performance of the resulting CuO thin film are controlled by the crystal plane exposed on Cu_2O nanocrystals. These findings highlight the strong connection of atomic structures of catalyst surfaces before and after surface restructuring and reveal the novel concept of crystal-plane-controlled surface restructuring of nanocrystals in reactive environments, thus opening a new door for improving and designing efficient nanocatalysts.

Experimental Section

Copper(II) chloride dehydrate ($CuCl_2{\cdot}2H_2O$, AR), sodium hydroxide (NaOH, AR), L-ascorbic acid (AR), poly(vinylpyrrolidone) (PVP) and absolute ethanol (AR) were purchased from Sinopharm Chemical Reagent Co., Ltd. and used as received. Distilled water was made by the Water Purifier lab pure water system. All gases were of ultrahigh purity and were obtained from Nanjing Shangyuan Industrial Gas Factory, China.

Cuprous oxide nanocubes ($c\text{-}Cu_2O$) were synthesized as follows: NaOH aqueous solution (2.0 mol L^{-1}; 10 mL) was added dropwise into $CuCl_2$ aqueous solution (0.01 mol L^{-1}; 100 mL) at 55 °C. After stirring for 0.5 h, ascorbic acid solution (0.6 mol L^{-1}; 10 mL) was added dropwise into the solution. The resulting solution was stirred for 5 h at 55 °C. The resulting precipitate was collected by centrifugation and decantation and was then washed with distilled water and absolute ethanol, and finally dried under vacuum at RT for 12 h.

Cuprous oxide nanooctahedra ($o\text{-}Cu_2O$) were synthesized as follows: NaOH aqueous solution (2.0 mol L^{-1}; 10 mL) was added dropwise into $CuCl_2$ aqueous solution (0.01 mol L^{-1}; 100 mL) containing 8.88 g PVP ($M_w = 30000$) at 55 °C. After stirring for 0.5 h, ascorbic acid solution (0.6 mol L^{-1}; 10 mL) was added dropwise into the solution. The resulting solution was stirred for 3 h at 55 °C. The resulting precipitate was collected by centrifugation and decantation and was then washed with distilled water and absolute ethanol, and finally dried under vacuum at RT for 12 h.

Powder X-ray diffraction (XRD) patterns were recorded on a Philips X'Pert PROS diffractometer using a nickel-filtered $Cu_{K\alpha}$ (0.15418 nm) radiation source with the operation voltage and the operation current being 40 kV and 40 mA, respectively. BET surface areas were measured using Micromeritics Tristar II 3020M. The sample was degassed at 100 °C under vacuum prior to the measurement. X-ray photoelectron spectroscopy (XPS) measurements were performed on an ESCALAB 250 high performance electron spectrometer using monochromatized $Al_{K\alpha}$ ($h\nu = 1486.6$ eV) as the excitation source. The expected charging of samples was corrected by setting the C 1s binding energy of the adventitious carbon to 284.5 eV. Scanning electron microscope (SEM) experiments were performed on a JEOL JSM-6700 field emission scanning electron analyzer. Transmission electron microscope (TEM) and selective-area electron diffraction (ED) experiments were performed on a JEOL-2010 transmission electron microscope. H_2 temperature programmed reduction experiments (H_2-TPR) were conducted on Micromeritics ChmiSorb 2750. The catalyst (10 mg) diluted with SiO_2 powder (10 mg) was placed in a U-shaped tube and heated at the rate of 5 °C min^{-1}. 5% H_2 in Ar with a flow rate of 20 mL min^{-1} was used and the consumption of H_2 was detected by a thermal conductivity detector (TCD).

The catalytic activity of Cu_2O nanocrystals for the oxidation of CO was evaluated with a fixed-bed flow reactor. The catalyst (30 mg) diluted with SiO_2 (30 mg) was used and the reaction gas consisting of 1% CO in dry air was fed at a rate of 30 mL min^{-1}. The catalyst was heated to the desired reaction temperatures at a rate of 2 °C min^{-1} and then kept there for 50 min until the catalytic reaction reached a steady state. Then the composition of effluent gas was analyzed with an online GC-14 gas chromatograph. The conversion of CO was calculated from the change in CO concentration of the inlet and outlet gases.

Theoretical calculation method: All the calculations were performed by the DMol^3 package[24,25] with spin-polarized density functional theory (DFT). Double numeric polarization (DNP) basis sets, DFT semicore pseudopotential (DSPP), and PBE functional[26] were adopted to expand the wavefunctions, describe the interaction between a single electron and the nuclei, and describe the exchange-correlation potential for all the atoms. Similar with our previous work, 0.06 $Å^{-1}$ spaced k-point meshes were used. Thermal smearing and real-space cutoff is set as 0.002 Hartree and 4.4 Å, respectively. The transition state of each elementary step proceeding by the Langmuir-Hinshelwood mechanism was searched by combined linear and quadratic synchronous transit methods with conjugated gradient refinements[27] and that by the Eley-Rideal mechanism was searched by the constrained minimization method by changing the distance between the C atom and O atom step by step.

Received: May 31, 2011
Published online: October 26, 2011

Keywords: Cu_2O nanocrystals · nanocatalysis · oxidation · structure–activity relationships · surface chemistry

[1] G. Ertl, H. Knözinger, F. Schüth, J. Weitkamp, *Handbook of Heterogeneous Catalysis*, Wiley-VCH, Weinheim, **2008**.
[2] G. A. Somorjai, *Introduction to Surface Chemistry and Catalysis*, Wiley-VCH, Weinheim, **1997**.
[3] R. Imbihl, G. Ertl, *Chem. Rev.* **1995**, *95*, 697.
[4] J. D. Batteas, J. C. Dunphy, G. A. Somorjai, M. Salmeron, *Phys. Rev. Lett.* **1996**, *77*, 534.
[5] T. P. Pearl, S. J. Sibener, *J. Chem. Phys.* **2001**, *115*, 1916.
[6] H. Over, Y. D. Kim, A. P. Seitsonen, S. Wendt, E. Lundgren, M. Schmid, P. Varga, A. Morgante, G. Ertl, *Science* **2000**, *287*, 1474.
[7] J. Gustafson, A. Mikkelsen, M. Borg, E. Lundgren, L. Köhler, G. Kresse, M. Schmid, P. Varga, J. Yuhara, X. Torrelles, C. Quirós, J. N. Andersen, *Phys. Rev. Lett.* **2004**, *92*, 126102.
[8] F. Tao, S. Dag, L. Wang, Z. Liu, D. R. Butcher, H. Bluhm, M. Salmeron, G. A. Somorjai, *Science* **2010**, *327*, 850.
[9] Z.-P. Liu, P. Hu, A. Alavi, *J. Chem. Phys.* **2001**, *114*, 5956.
[10] X.-Q. Gong, R. Raval, P. Hu, *Phys. Rev. Lett.* **2004**, *93*, 106104.
[11] B. L. M. Hendriksen, S. C. Bobaru, J. W. M. Frenken, *Surf. Sci.* **2004**, *552*, 229.
[12] J. Rogal, K. Reuter, M. Scheffler, *Phys. Rev. Lett.* **2007**, *98*, 046101.
[13] A. F. Lee, C. V. Ellis, J. N. Naughton, M. A. Newton, C. M. A. Parlett, K. Wilson, *J. Am. Chem. Soc.* **2011**, *133*, 5724.
[14] F. Tao, M. Salmeron, *Science* **2011**, *331*, 171.
[15] C. R. Henry, *Surf. Sci. Rep.* **1998**, *31*, 231.
[16] P. L. Hansen, J. B. Wagner, S. Helveg, J. R. Rostrup-Nielsen, B. S. Clausen, H. Topsøe, *Science* **2002**, *295*, 2053.
[17] P. Nolte, A. Stierle, N. Y. Jin-Phillipp, N. Kasper, T. U. Schulli, H. Dosch, *Science* **2008**, *321*, 1654.
[18] E. K. Vestergaard, R. T. Vang, J. Knudsen, T. M. Pedersen, T. An, E. Lægsgaard, I. Stensgaard, B. Hammer, F. Besenbacher, *Phys. Rev. Lett.* **2005**, *95*, 126101.
[19] J. Zhang, K. Sasaki, E. Sutter, R. R. Adzic, *Science* **2007**, *315*, 220.
[20] F. Tao, M. E. Grass, Y. Zhang, D. R. Butcher, J. R. Renzas, Z. Liu, J. Y. Chung, B. S. Mun, M. Salmeron, G. A. Somorjai, *Science* **2008**, *322*, 932.

[21] E. de Smit, I. Swart, J. F. Creemer, G. H. Hoveling, M. K. Gilles, T. Tyliszczak, P. J. Kooyman, H. W. Zandbergen, C. Morin, B. M. Weckhuysen, F. M. F. de Groot, *Nature* **2008**, *456*, 222.
[22] G. Yu. B. Sun, Y. Pei, S. Xie, S. Yan, M. Qiao, K. Fan, X. Zhang, B. Zong, *J. Am. Chem. Soc.* **2010**, *132*, 935.
[23] H. Z. Bao, W. H. Zhang, D. L. Shang, Q. Hua, Y. S. Ma, Z. Q. Jiang, J. L. Yang, W. X. Huang, *J. Phys. Chem. C* **2010**, *114*, 6676.
[24] B. Delley, *J. Chem. Phys.* **1990**, *92*, 508.
[25] B. Delley, *J. Chem. Phys.* **2000**, *113*, 7756.
[26] J. P. Perdew, K. Burke, M. Ernzerhof, *Phys. Rev. Lett.* **1996**, *77*, 3865.
[27] N. Govind, M. Petersen, G. Gitzgerald, D. King-Smith, J. J. Andzelm, *Comput. Mater. Sci.* **2003**, *28*, 250.

